SANDIA REPORT
SAND2020-10945
Printed Click to enter a date

Design for Additive Manufacturing: Exploring Remelt Strategies to Tailor Density and Microstructure

Jonathan Pegues, Theron Rodgers, Shaun Whetten, Will Dannemann, David Saiz, Andrew Kustas

Prepared by
Sandia National Laboratories
Albuquerque, New Mexico
87185 and Livermore,
California 94550

Issued by Sandia National Laboratories, operated for the United States Department of Energy by National Technology & Engineering Solutions of Sandia, LLC.

Available to DOE and DOE contractors from
U.S. Department of Energy
Office of Scientific and Technical Information
P.O. Box 62
Oak Ridge, TN 37831

Telephone: (865) 576-8401
Facsimile: (865) 576-5728
E-Mail: reports@osti.gov
Online ordering: http://www.osti.gov/scitech

Available to the public from
U.S. Department of Commerce
National Technical Information Service
5301 Shawnee Rd
Alexandria, VA 22312

Telephone: (800) 553-6847
Facsimile: (703) 605-6900
E-Mail: orders@ntis.gov
Online order: https://classic.ntis.gov/help/order-methods/

ABSTRACT

The potential advantages of AM (e.g. weight reduction, novel geometries) are well understood within a systems context. However, adoption of AM at the system level has been slow due to the relative uncertainty in the final material properties, which leaves capabilities and/or performance gains unrealized. Utilizing remelt strategies it may be possible to expand the available process window to provide densities and microstructures beyond what is capable with standard scan strategies. This work explored remelting strategies for 316L stainless steel to tailor grain size and increase density. Twelve scan strategies were explored experimentally and computationally to understand the limitations of remelt strategies and the robustness of the current simulation package. Results show tailoring of grain size, density, and texture is achievable through remelting and several key lessons learned were made to improve the texture evaluation through simulation.

ACKNOWLEDGEMENTS

The authors acknowledge Luis Jauregui for microstructure characterization, Celedonio Jaramillo and Jacob Mahaffey for metallographic preparation of specimens, Seethambal Maniand for guidance throughout the project, and RDCS/Tech maturation portfolio for providing funding for this research.

CONTENTS

LIST OF FIGURES

LIST OF TABLES

This page left blank

ACRONYMS AND DEFINITIONS

Abbreviation	Definition
AM	additive manufacturing
EBSD	electron backscatter diffraction
EDS	energy dispersive x-ray spectroscopy
FE-SEM	field emission scanning electron microscope
KDE	Kernel Density Estimates
LB-PBF	laser beam powder bed fusion
NDI	non-destructive inspection
SPPARKS	stochastic parallel particle kinetic simulator

1. INTRODUCTION

Additive manufacturing (AM) is a rapidly maturing technology which will inevitably be implemented to fabricate structural components. Survivability of these components depends on the ability to circumvent the effects of process induced defects such as porosity and improve reliability in additive manufactured hardware. Among the most sensitive mechanical properties to the process induced defects common to the additive manufacturing process is the fatigue strength [1, 2]. Gas entrapped porosity and lack of fusion type defects that occur during the AM process introduce discontinuities with sharp features that effectively increase local stress responses promoting early life crack initiation which ultimately results in poor fatigue performance for these materials [3-5]. Much effort has targeted closing the knowledge gap related to the process-structure-property relationships of AM materials to improve the fusion process and reduce/minimize porosity. Despite these valiant efforts, the uncertainty related to fatigue performance is still high as the critical defect size for fatigue is on the order of 10s of microns, which is impractical to identify through non-destructive inspection (NDI) techniques. Despite these challenges the value proposition provided by AM is attractive across many industries and therefor methods to improve confidence in performance in fatigue critical applications is necessary.

One benefit provided by AM that is often overlooked in design is the ability to control local thermal history through the processing parameters. The microstructure morphology is directly associated with the thermal history and solidification behavior which essentially opens the door for direct control over the local microstructure [6]. This unprecedented influence of the local microstructure while simultaneously forming the net geometry creates a paradigm shift in engineering design process. Through AM it is possible to design microstructures in specific locations to target expected failure modes associated with the physical loads expected. For fatigue applications, this design for AM can be leveraged to generate site specific microstructures and densities to minimize local deformation and extend the life to nucleate a microcrack. Previous work on additive manufactured 304L stainless steel has demonstrated the benefit of AM for bulk material [7, 8], i.e. not spatially graded microstructures, to improve fatigue resistance beyond what is expected for wrought material. It is generally accepted that fine microstructures are favorable to limit dislocation motion which have long been attributed to micro crack formation by dislocation pileup at discontinuities. On the other hand, large grains are typically desired once a crack reaches the microstructurally short regime of crack growth in order to deflect the crack and increase the surface energy that must be overcome to extend the crack. Extending this thought process to a component, it is conceivable to adjust process parameters at a given geometrical feature that promotes crack initiation to acquire fine grain sizes and increased resistance to crack initiation. Away from these local stress risers, parameters can then be adjusted to provide larger grain sizes targeting crack deflection once a crack has initiated and developed into a short crack. This thought exercise demonstrates the value of AM to provide site-specific microstructure/properties to ultimately improve the performance of the part beyond what is achievable through conventional processes.

The first step in exploring a spatially gradient approach for improving fatigue performance is understanding the available microstructure window afforded by the AM process. The hierarchy of fatigue sensitive features attributed to AM is surface roughness, defect structure, then microstructure, such that the benefits/issues of microstructure are often overshadowed by roughness and porosity [9]. This hierarchy suggests that, before microstructural control can be leveraged in a spatially gradient approach, the effect surface roughness and defect structure must be minimized to the extent the microstructure influences the fatigue behavior. While in general surface roughness can be removed through post-process surface treatments without significantly affecting the microstructure, post-processes capable of affecting the defect structure inevitably affect the resulting microstructure and can adversely affect the mechanical performance [8]. This means that in order to take advantage of microstructural control through the AM process, the defects common to these platforms must be minimized during the AM process.

Several studies have documented the challenges and opportunities associated with surface roughness effects on the fatigue behavior of AM parts [10-14]. In fact, the uncertainty related to the fatigue behavior of AM parts with quantifiable surface topography has been shown to be low, with predictive models showing success for Ti-6Al-4V and 304LSS [12, 15]. When the surface is removed, however, defects become the dominate factor in fatigue strength and the nature of this effect is stochastic [16]. This often leads to fatigue results within a given stress/strain range to have unpredictable variations between data points often exceeding two orders of magnitude. This is related to the severity of the defect being attributed not only to its size but also distance from the surface and geometrical features, such as sharpness. All these affects combine to determine the criticality of a given defect. In order to minimize the uncertainty of fatigue resistance related to defects either the part must be evaluated by NDI or the process conditions need to be improved to minimize the porosity, particularly in regions identified as promoting high stresses.

As mentioned previously, NDI can be an impractical method for inspection for fatigue critical components larger than a standard test coupon. This is due to the critical size of the defects to initiate cracks tends to be on the order of 10s of microns which requires XCT fields of view to be extremely small. This means the most practical solution to improving confidence in the fatigue resistance of AM parts is tuning the process parameters to provide material with minimal porosity. As such, much work has been done in the field of process optimization given a processing window [17-19]. One of the most promising processing approaches aimed at minimizing porosity has been remelting of previously solidified layers. Several works have shown that multiple remelt passes can heal defects that formed or were trapped during the initial fusion process [20, 21].

This work explores remelting as a design consideration to minimize porosity while providing microstructural control to the resulting solidified structure. Several process parameters are investigated both within and outside the typical process window for 316L stainless steel produced by laser beam powder bed fusion. The remelting scan strategies are evaluated based on their capability to reduce porosity, control grain size, and influence texture.

2. EXPERIMENTAL METHODS

A ProX 200 LB-PBF system was utilized to explore the melt pool characteristics and fabricate several metallurgical cubic samples. To improve density, several remelt process parameters were also selected based on the melt pool characteristics expected to provide target microstructures. Small melt pool sizes were utilized to target fine grain sizes while larger melt pools targeted larger grain sizes. Line scans reported in [cite if available] were used to assess the associated melt pool size and to select a range of process parameters targeting fine to coarse grain sizes. These results are shown in Figure 1 with power law fits for each dimension. These relationships were used to select remelt laser parameters capable of providing fine or coarse grain sizes. In general, the overlap depth between adjacent melt pools should be at least twice the layer thickness for a stable process condition [22, 23]. However, for remelt passes this requirement was considered less stringent as the point of the material-laser interaction is more stable since the material is consolidated and spatter events from ejected powder particles are minimized. As such, the remelt pass the overlap depth was minimized to approximately the layer thickness. The process parameters for both fusion (1st pass) and remelt (2nd pass) are detailed in Table 1.

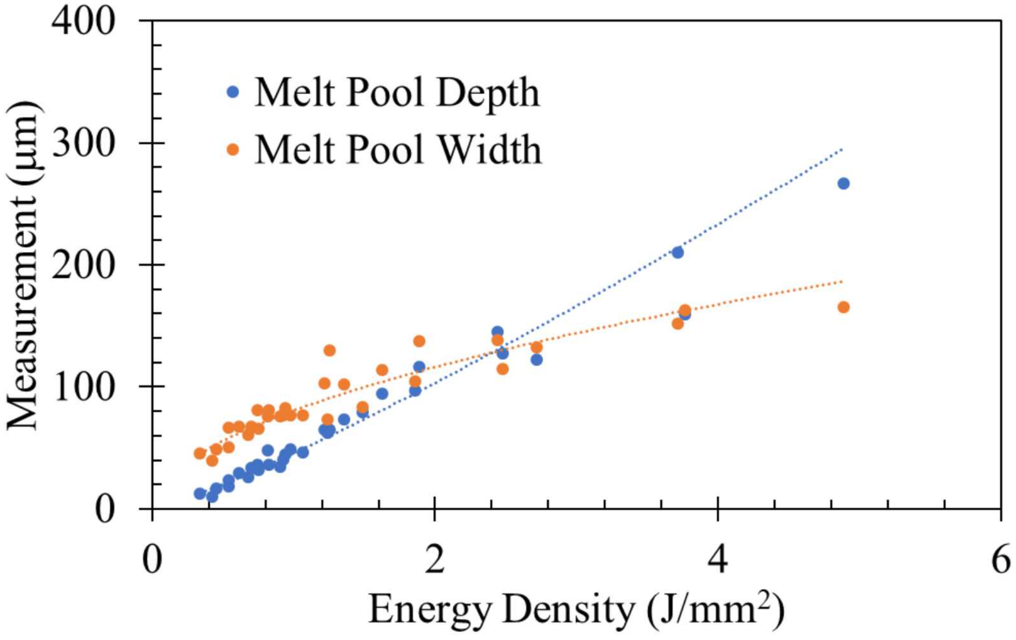

Figure 1: Melt pool depth and widths for the associated energy densities with corresponding power law fits.

Table 1: Fusion and remelt parameters for each metallurgical sample.

	Fusion-1st Pass				Remelt-2nd Pass			
	Power (W)	Velocity (mm/s)	Layer (μm)	Hatch (μm)	Power (W)	Velocity (mm/s)	Layer (μm)	Hatch (μm)
Sample 01	90	1400	30	50	-	-	-	-
Sample 02	200	1400	30	50	-	-	-	-
Sample 03	140	1800	30	50	-	-	-	-
Sample 04	120	1000	30	50	-	-	-	-
Sample 05	90	1400	30	50	90	1400	30	50
Sample 06	90	1400	30	50	175	1250	30	77
Sample 07	140	1800	30	50	90	1400	30	50
Sample 08	140	1800	30	50	175	1250	30	77
Sample 09	200	1400	30	50	90	1400	30	50
Sample 10	200	1400	30	50	175	1000	30	100
Sample 11	120	1000	30	50	90	1400	30	50
Sample 12	120	1000	30	50	175	1000	30	100

The metallurgical samples were sectioned and mounted in cold-set epoxy for microstructural characterization and mechanical properties analysis. The sectioned samples were mounted to show the longitudinal (parallel with build direction) plane and the transverse (perpendicular to build direction) plane. The mounted specimens were ground with SiC paper and then polished with a 1 μm diamond suspension. To achieve a surface finish optimal for EBSD analysis, two vibratory polishing steps were employed with a 0.3 μm Al_2O_3 slurry followed by a 0.04 μm SiO_2 slurry. High resolution microstructure analysis was done on a Zeiss Supra 55-VP field emission scanning electron microscope equipped with Oxford Instruments EDS (X-Max SDD) and EBSD (Symmetry) detectors. All imaging was performed with an acceleration voltage of 20 kV.

AM microstructures were simulated using the stochastic parallel particle kinetic simulator (SPPARKS) microstructure simulation code[24]. Several iterations of AM microstructure simulation have been realized in SPPARKS. Here, we focus on a method that directly couples a finite difference-based thermal conduction solver with a Monte Carlo-based solidification model for microstructure evolution. Unlike initial SPPARKS AM models, which used a modified Potts Monte Carlo method, the current method uses a solidification-theory based approach that directly incorporates physics such as grain nucleation and undercooling-dependent solidification front velocity. More information on the model can be found in [25].

Additionally, the approach incorporates crystallographic texture-dependent solidification behavior for alloys with cubic crystal lattices. This method leverages the knowledge that these materials solidify fastest in the [100] crystal direction. Thus, grains who have a well-aligned [100] axes will outcompete neighboring grains with less-optimal orientations. Modifications to the model were also required to enable layer remelting with different laser parameters as studied in builds 5-12 and the offset remelt strategy of builds 5, 7, 9, and 11.

3. EXPERIMENTAL RESULTS

3.1. Porosity Analysis

Remelt strategies revealed surprising results on the final porosity measurements of the various metallurgical samples. Table 2 list the maximum and average porosity size for each condition along with the primary fusion parameter sets (1st pass) provided for comparison. All remelt strategies resulted in a reduction in maximum pore size and 6 out of the 7 resulted in a reduction of the average pore size, suggesting remelting is effective in reducing porosity. For standard single pass scan strategies (samples 01-04), process 02 resulted in the smallest average porosity size while process 03 had the largest. Interestingly, the benefit of remelting after utilizing the fusion parameters associated with sample 02 fusion parameters was minimal as indicated by sample 09 showing a slight increase in average pore size. Remelting after process 01, however, showed approximately 60-80% reductions in average pore size and resulted in an average pore size of 1.0 μm^2 and a maximum of 14.2 μm^2. Another interesting observation is that despite reductions in porosity reaching 69-81% for remelting associated with fusion process 03, the average porosity size was large than the single pass process of sample 02. This observation implies the benefit of remelting is limited by the pore sizes achieved during the fusion pass as process 03 showed the highest maximum and average pore sizes of all single pass process parameters.

Table 2: Porosity results associated with the various fusion and remelt energy densities.

Sample #	Fusion Energy (J/mm^2)	Remelt Energy (J/mm^2)	Max Pore Size (μm^2)	Average Pore Size (μm^2)	Standard Dev.	% Change %
01	0.64	-	848.3	6.2	48.6	-
02	1.43	-	132.7	2.2	8.8	-
03	0.78	-	1085.2	12.8	64.6	-
04	1.20	-	504.3	4.7	35.1	-
05	0.64	0.64	87.2	2.5	5.8	-60
06	0.64	1.40	14.2	1.0	1.6	-83
07	0.78	0.64	91.3	4.0	9.9	-69
08	0.78	1.40	54.8	2.5	6.8	-81
09	1.43	0.64	52.4	2.2	5.2	+06
11	1.20	0.64	14.2	1.2	2.1	-74
12	1.20	1.75	13.0	1.2	2.0	-75

Interestingly, the lowest observed porosity was not associated with the fusion process 02. Instead the lowest porosity was obtained for coupon 06 and 12 which had the lowest average porosity size and lowest maximum porosity size respectively. In both of these remelt strategies a lower energy fusion pass is followed by a higher energy remelt pass. The higher energy density remelt passes penetrate deeper which may provide greater opportunity to affect pores within the previously solidified layer.

3.2. Microstructural Characterization

EBSD results and average equivalent grain diameters for the fusion process conditions are shown in Figure 2. For all process conditions the checkerboard pattern associated with 90° laser track rotation is observed. For these process conditions the highest to lowest supplied energy density is in order samples 02, 04, 03, and 01. Coincidentally, the grain size from largest to smallest follows the same order, highlighting the relationship between energy density, melt pool size, and the solidified microstructure. The increase in grain size from sample 01 (Figure 2(a)) to sample 02 (Figure 2(b)) is around 133%, demonstrating a substantial level of grain size control from the fusion parameters alone.

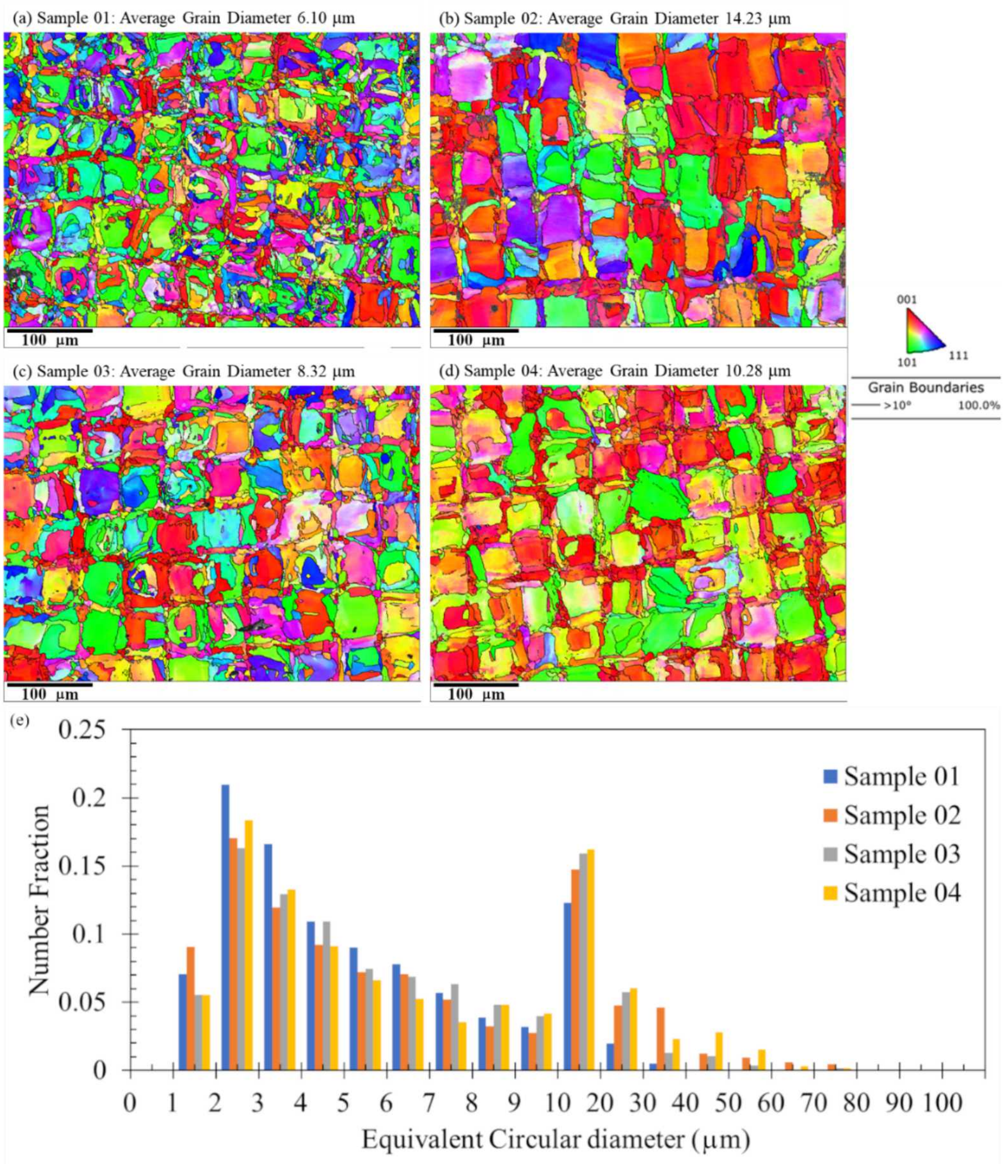

Figure 2: EBSD results and associated grain sizes for the standard fusion parameters for samples (a) sample 01, (b) sample 02, (c) sample 03, (d) sample 04, and (e) their associated grain size distribution.

One interesting thing to note on the grain size distribution is that the average grain size is skewed to the lower end, due to the high number of grains with diameters below 10 μm. Binning the grain sizes in a logarithmic pattern as shown in Figure 2(e), the differences in size distributions are more evident. Observations of samples 02 and 04 indicate that a much larger average grain size than reported would be expected. When comparing the grain size distributions in Figure 2(e) the higher density of grains > 10 μm is apparent for samples 02 and 04. This suggest that despite the low average grain sizes (between 10-14 μm) for samples 02 and 04, the microstructure is heavily influenced by grains larger than 10 μm.

The effect of the various remelting strategies on the final grain size and texture for similar fusion parameters was of interest in this study. As such, the grain size and texture of the remelt strategies and the associated single pass samples were directly compared. Figure 3 shows the resulting microstructure characteristics for the first pass parameter set associated with process 01. Figure 3(a) is the standard single pass scan strategy while Figure 3(b)&(c) included remelt passes. The goal of the remelt strategy for sample 05 was to reduce porosity while maintaining or further reducing the small average grain size. The porosity results demonstrated success in increasing density, which showed a decrease of 60% from sample 01. The grain size was also refined from ~6 μm equivalent diameter to ~4.75 μm which is about a 22% reduction. While the remelt did increase the texture slightly from sample 01, the maximum 3.86 times the random is considered as a weak texture and is not expected to cause severe anisotropy in the material.

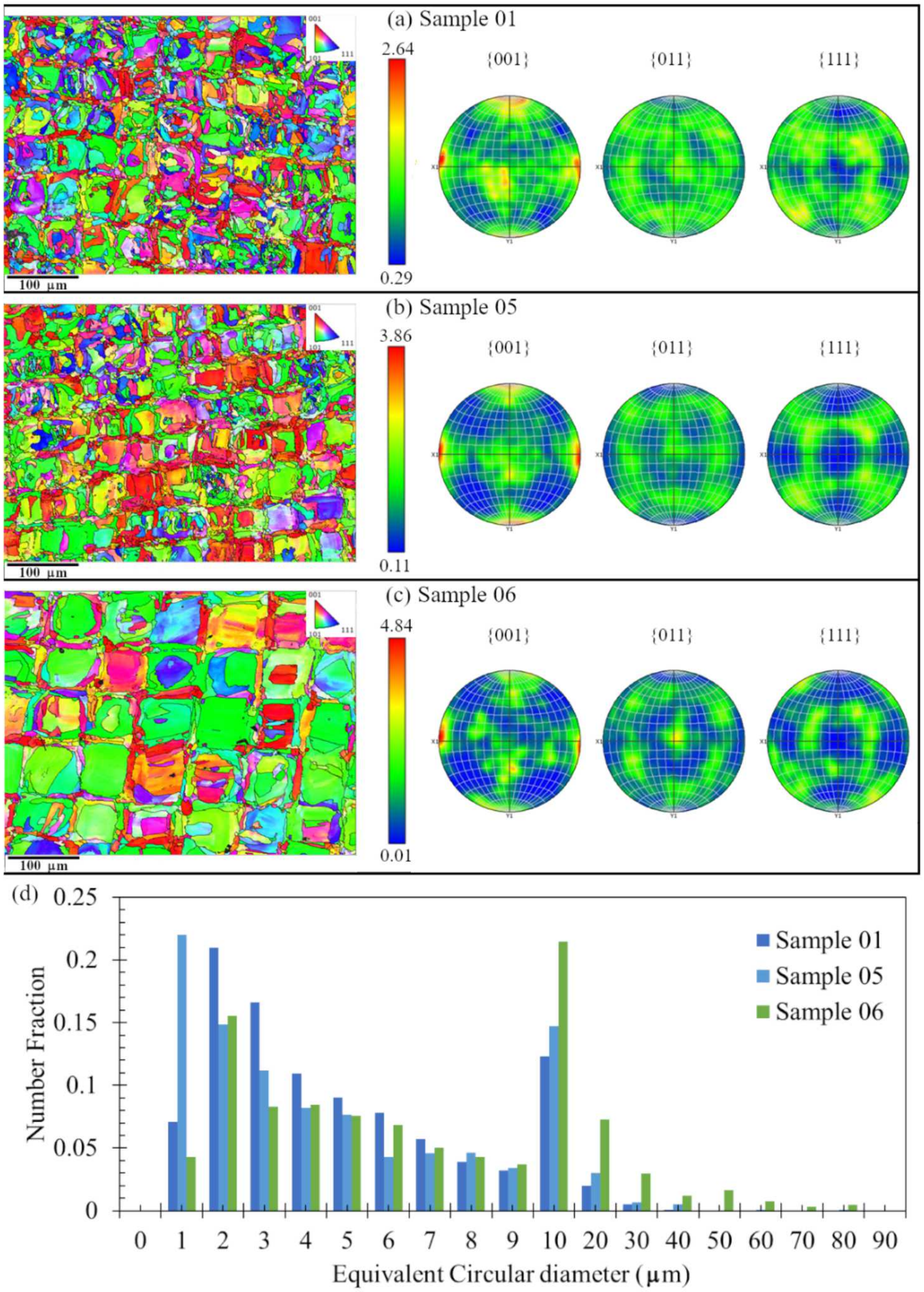

Figure 3: EBSD results and texture analysis for (a) standard fusion process 01, and associated remelt strategies for the (b) sample 05, and (c) sample 06, and (d) their respective grain size distributions.

The remelt strategy for sample 06 in Figure 3(c) was also to improve density while achieving a larger grain size. As mentioned in the previous section, sample 06 had the lowest average porosity of all scan strategies, and successfully increased the average grain size from ~6 μm to ~11 μm an increase of about 84%. Again, the small average grain size is skewed to the lower end with the microstructure being dominated by grains larger than 10 μm. For this scan strategy the weak {001} texture of sample 01 shifted to a slightly stronger {011} texture which had a maximum of 4.84 times the random. The shift from a {001} to a {011} texture indicates the higher energy density is promoting a deeper melt pool such that the solidification front is not perpendicular to the build direction as shown in [26].

Sample 02, which resulted in the lowest porosity of the standard single pass scan strategies, had the largest average grain size of the standard scan strategies and a moderate {001} texture 5.3 times the random, shown in Figure 4(a). The remelting stratagies for process 09 in Figure 4(b) targeted lower porosity and a decrease in average grain size. While the porosity results were essentially the same between sample 02 and 09, the remelt strategy was succesful in reducing the average grain size from ~14 μm to ~11 μm or around 5%. The grain size distribution in Figure 4(c) suggests the grain size between these two strategies are similar. In addition to the grain size distribution, the texture of the two scan strategies are also similar. Sample 10 targeted increasing the average grain size but failed due to a recoater crash during fabrication and grain size data was not obtained.

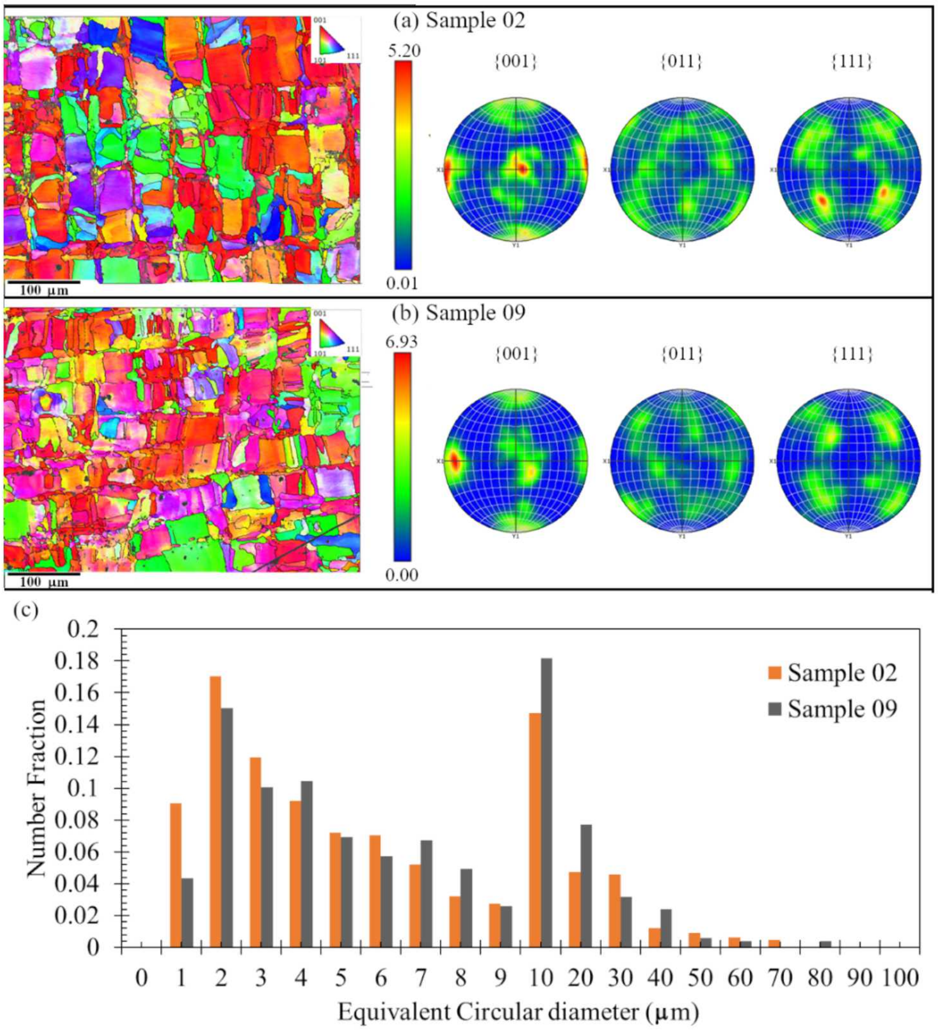

Figure 4: EBSD results and texture analysis for (a) standard fusion sample 02, associated remelt strategies for the (b) sample 09, .and their respective grain size distributions.

Sample 03 which had the highest porosity and low average grain size is compared to its associated remelt scan strategies in Figure 5. Like sample 01 the texture is low, only ~3 time the random. The remelt scan strategy for sample 07 in Figure 5(b) targeted lower porosity while maintaining small grain size. Despite a decrease in average pore size of ~70% sample 07 had the highest maximum and average pore size of all remelt strategies and resulted in a relatively small increase in grain size from ~8 μm to ~11 μm. Comparing the grain size distribution to sample 03, however, suggests there is no significant difference between these conditions. The texture for sample 07 did show a stronger alignment in the {001} direction but this is also considered a weak texture and not expected to promote strong anisotropy in the material.

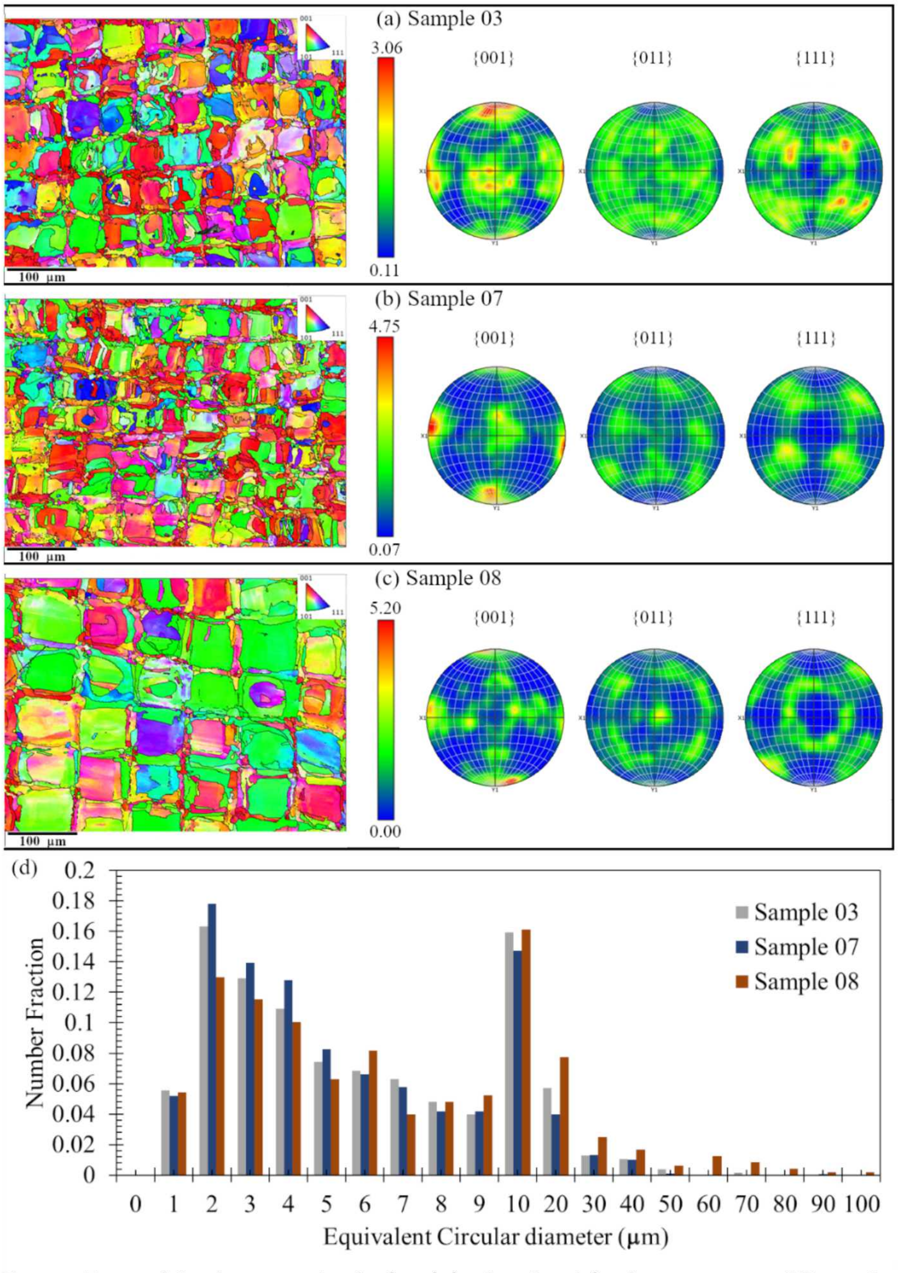

Figure 5: EBSD results and texture analysis for (a) standard fusion process 03, and associated remelt strategies for the (b) sample 07, (c) sample 08, and (d) their respective grain size distributions.

The remelt strategy for sample 08 was to increase grain size in conjunction with reducing the porosity. The average pore size was reduced by ~77% but like sample 07 it was still among the highest porosity sizes of all the remelt strategies. The grain size was successfully increased but had a similar average grain size to sample 07. The grain size distribution, however, suggests that sample 08 is statistically different than both sample 03 and 07 and is dominated by grain sizes larger than 10 μm. Similar to the higher energy density scan strategy in sample 06, sample 08 revealed a shift in weak texture from near the {001} pole to the {011} poles. The texture is rather weak however at approximately 4 times the random and is therefore not expected to significantly affect the isotropic behavior of the material. Despite the relative success in grain size control for samples 07 and 08 the poor porosity improvements make these scan strategies less attractive than others in this study.

Sample 04 had the second lowest porosity of the standard single pass process parameters, second largest grain size, and a moderate {001} texture as indicated in Figure 6(a). The remelt strategy for sample 11 was again to reduce porosity while maintaining/refining the average grain size. Both the average and maximum porosity sizes were near the lowest observed for all scan strategies and the grain size was reduced by about 5% from sample 04. There was only a slight increase in texture from sample 04. The grain size distribution in Figure 5(d) suggest that these grain sizes are not statistically different.

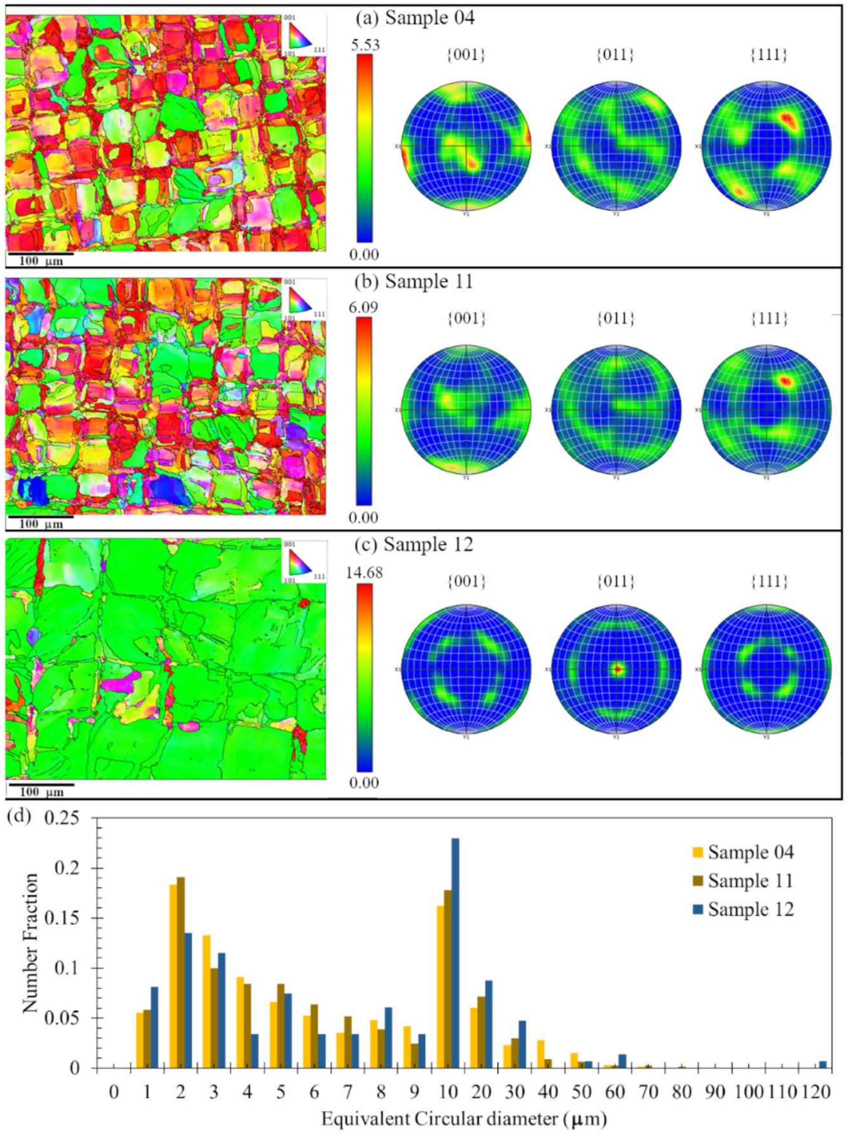

Figure 6: EBSD results and texture analysis for (a) standard fusion process 04, and associated remelt strategies for the (b) sample 11, (c) sample 12, and (d) their respective grain size distributions.

The remelt strategy for sample 12 again was to increase grain size while reducing the porosity. The average grain size revealed only a moderate 22% increase in grain size, however, visually comparing the microstructures of sample 04 (Fig. 6(a)) and sample 12 (Fig. 6(c)) suggest a much greater influence on the grain size. The grain size distribution shown in Figure 6(d) indicates that the microstructure of sample 12 is dominated by grains larger than 10 μm and contained the largest grains observed for all samples. In addition to the large effect on grain size, the largest remelt energy density associated with sample 12 also resulted in a severe texture along the {011} pole ~15 times the random. This strong texture would be expected to result in anisotropic behavior for this scan strategy.

3.3. Simulation Results

The simulation parameters used for the 316L stainless steel samples were the same as utilized for the experiments provided in Table 1. Thermal properties were taking from [27] while solidification parameters were adapted from [11]. The laser spot was represented as a 3D Gaussian with parameters from the experimental plan in Table 1. Laser raster paths were also specified to match those from experiment Table 1. Initial simulations were performed with a 10 x 10 x 10 mm domain, but this was found to be more than adequate to create representative bulk microstructures. The simulation volume was scaled back to 2.5 x 2.5 x 5 mm to reduce computational cost. A 10 μm lattice site resolution was also used to improve efficiency. Based on the experimental EBSD data, this resolution should be fine enough to resolve relevant microstructure features and can properly represent the nucleation site density value used here. Although the resolution limits the shape accuracy of small grains and likely skews the results to slightly larger grain sizes compared to experimental.

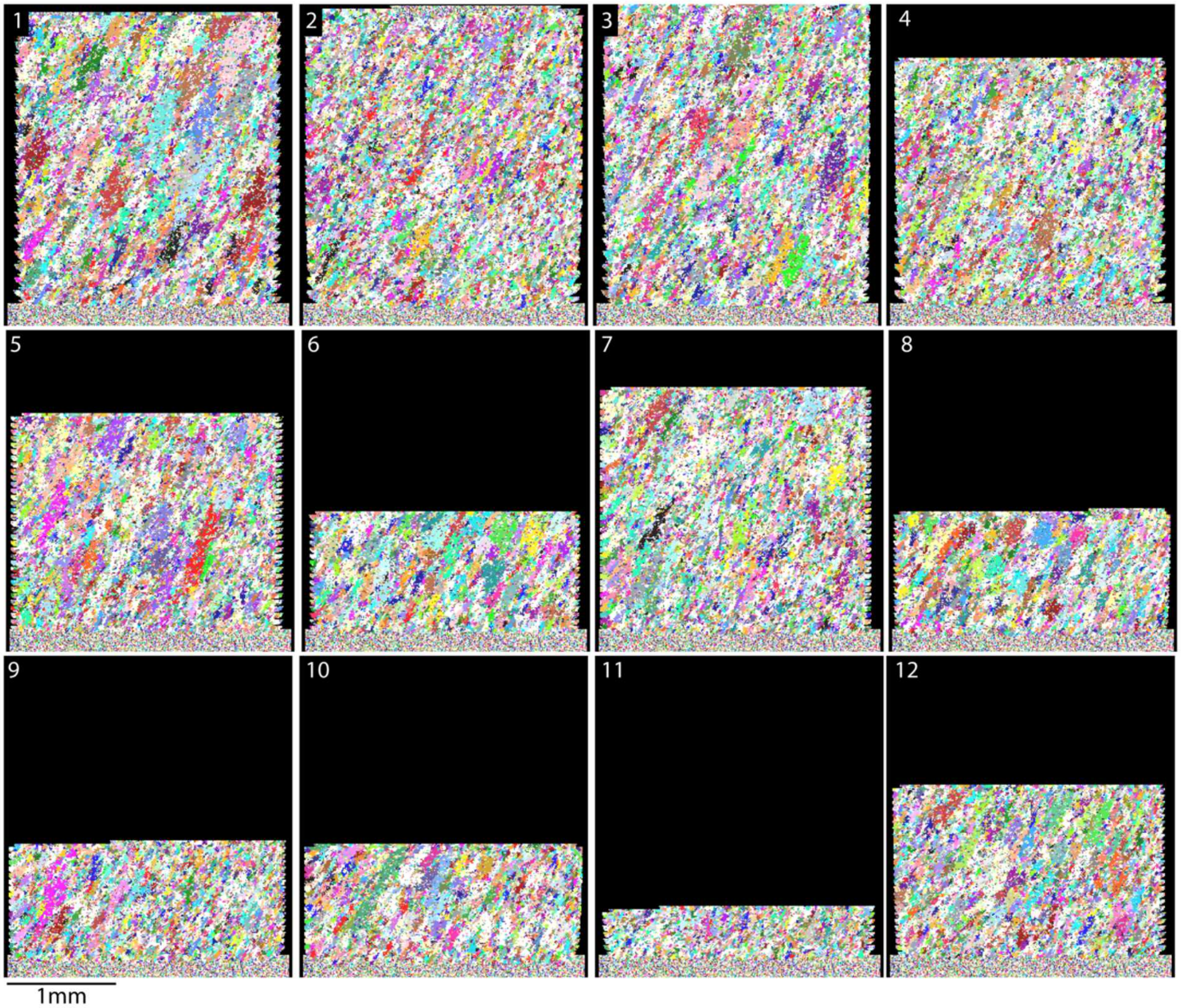

Figure 7: Cross-sections of simulated microstructures for conditions 1-12. Conditions 1-4 involved no remelting, while conditions 5-12 had some form.

Cross-section images of the microstructures for the builds of interest are shown in Figure 1. Columnar grains mixed with equiaxed nucleated grains are present in all microstructures. Remelted domains tend to have larger grains than the single pass builds. Columnar grains also tend to be tilted away from the build direction, which was likely caused by inadequate cooling times between laser rasters or laser raster patterns with incorrect rotation schemes. It is also noticeable in Figure 1 that the segmented microstructures have different thicknesses. All simulations except for Build 11 were performed for roughly the same amount of "experimental" time. Build time is impacted by the use of remelting and the laser scan speed. Additionally, the simulated time between layers is dependent on local cooling rates of the melt pool. Between each layer, the simulation waits for the maximum temperature to decrease below the solidus value. Thus, "hotter" simulations will have longer recoating times.

Grain size distributions of the microstructures created at conditions 1-4, 5, 7, and 12 are shown in Figure 8. Substrate material was removed from the analysis. The plots show the kernel density estimate of volume-weighted fraction of the equivalent spherical diameter of simulated grains. All simulations had a similar result with a peak near ~25-50 μm and with long tails at larger sizes. The peak at small grain sizes results from small grains nucleating during solidification with the larger grain sizes compared to the experiments likely originating from the 10 μm resolution. Nucleated grains are much smaller than epitaxially-grown columnar grains and result in a peak at small grain sizes. The magnitude of small grain volume fraction varied significantly between simulations. Build 1 had the smallest fraction of nucleated grains. This condition had a small melt pool with large thermal gradients that reduced grain nucleation. The largest fraction of nucleated grain was found in Build 2. In this simulation, the dwell time between subsequent laser passes was too short to allow full cooling of the simulation domain. This resulted in melt pools from consecutive passes joining together and creating a large melt pool with lower thermal gradients and solidification rates. All distributions had long tails of similar intensities, which indicates that large grains were prevalent in all results. However, there was not a preferred grain size as found for the nucleated grains. Another complicating factor with the microstructure analysis is that many larger grains go through the thickness of the deposit. The different microstructures had differing thicknesses, which resulted in different maximum grain sizes for each structure.

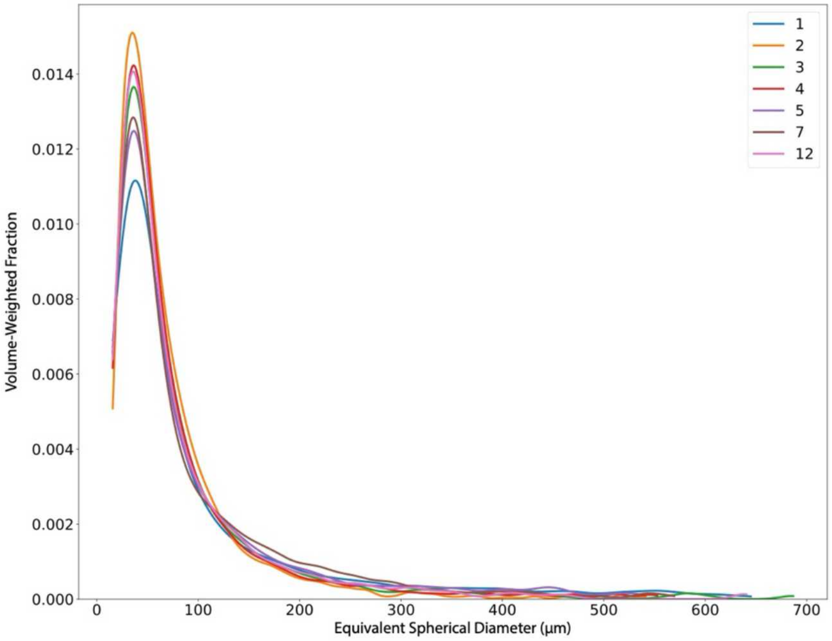

Figure 8: Kernel Density Estimates (KDE) of grain size distributions for the select scan strategies.

Pole figures for simulations 1-4, 5, 7, and 12 are shown in Figure 9. All simulations show weak but noticeable textures with maxima around 1.3 multiples of random. The weak texture results from the un-calibrated grain solidification rules used in the simulation. Ongoing work by collaborators at Carnegie Melon University indicate that the simulation method is capable of reproducing accurate textures but tends to underpredict intensity without calibration. Future work will leverage the work at CMU to improve model accuracy [28].

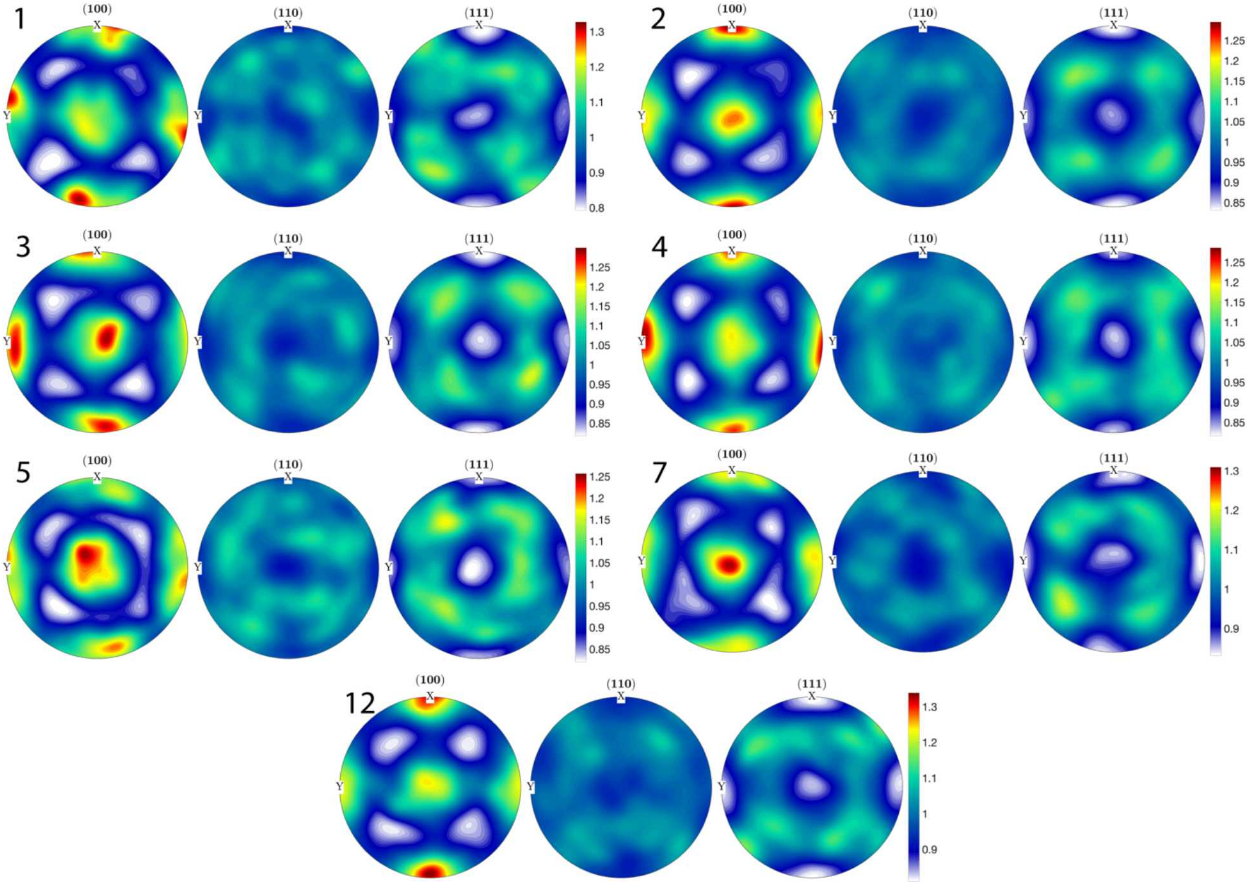

Figure 9: Simulated pole figures. The Z-direction corresponds to the build direction.

4. DISCUSSION

Experimental results suggest remelting strategies can expand the process window to achieve greater control over the final density, grain size, and texture. These material characteristics can provide insight towards mechanical performance of parts utilizing these advance scanning strategies and the increased tunability of the final material properties afforded by remelting. Most importantly the reduction in porosity is critical to many mechanical properties as these discontinuities typically lead to early crack initiation and ultimately affect ductility, fatigue strength, and fracture toughness. Porosity is often attributed to the uncertainty in mechanical performance associated with AM materials so minimizing the presence of these pores is critical to their reliability for most structural applications.

Comparing the smallest average pore size achieved for single pass scanning strategies to the smallest achieved from remelt scanning strategies, there is greater than 50% reduction in favor of remelting. While this reduction in average porosity is a positive sign for mechanical performance, fatigue failure is a highly local phenomena and is influenced by the most severe defect which is often correlated to the largest pore. In this case it is important to consider the effect on the maximum pores size in addition to the average pores size. Sample 06, which resulted in the biggest decrease in average pore size (~83% compared to its single pass counterpart) showed an even more impressive reduction in maximum pore size of ~98%. While the reduction in maximum pore size for samples 11 and 12 were not as impressive as sample 07, they had the lowest maximum pore sizes of 14.8 and 13 μm respectively.

More importantly for austenitic stainless steels, this reduction in pore size was accomplished without significantly impacting the fine grain size achieved for the low energy fusion parameters. Austenitic stainless steels cannot be strengthened by heat treatment and require cold working to increase strength. Cold working, however, imparts sever deformation into the material severly impacting its ductility. Considering the Hall-Petch relationship between grain size and strength, it would be beneficial for high strength applications to maintain the low grain sizes of coupons 01 and 03 while refining the grain sizes of coupons 02 and 04 through remelting. Remelt strategies associated with sample 01 and 03 demonstrated the ability to reduce porosity and maintain fine grain sizes, i.e. samples 05 and 07. On the other hand, the remelt strategies for sample 09 and 11 were able to reduce the average grain sizes associated with their fusion passes, 02 and 04 respectively, while also reducing porosity. These results suggest additive manufacturing of austenitic stainless steels could provide both improved fatigue resistance and tensile strengths without severely impacting the ductility performance of the material.

Remelt strategies aimed at increasing grain size also showed similar success. This success, however, must be balanced with the observation of increasingly strong {011} textures which can lead to severe anisotropic mechanical behavior. Interestingly, all remelt strategies utilizing an energy density of 1.4 J/mm^2 or greater resulted in a weak to moderate {011} texture while lower remelt energy densities resulted in a weak {001} texture. This is attributed to the melt depth to width ratio, where shallow-wide melt pools promote a {001} texture while deeper melt pools promote {011} texture. These results agree with previous work on LB-PBF 316L SS describing melt pool shape and resulting textures [26].

One key aspect of this work was assessing the ability of simulation to predict the effects of remelting on the final microstructure. Having a computational tool to accurately predict the resulting microstructure would allow for additional tuning of the process to optimize remelting strategies without the time and monetary burden of experimentation. The simulation study resulted in several lessons-learned that will be applied in future work. The finite-difference based method used here is desirable to predict the influence of variable laser process parameters and microstructure formation in non-uniform environments (such as near the edge of the build). However, more computationally efficient methods of representing meltpool dynamics (such as using approximate Rosenthal solution heat sources) improve the ability to quickly predict bulk microstructure features. The study also provided information regarding the optimal simulation volume to predict bulk AM microstructures. Smaller non-build dimensions allow for the rapid simulation of taller build heights. However, care must be taken to ensure that accurate melt pool dynamics are preserved. If short "turn around" times are used between each laser raster, heat can build up within the domain and prevent accurate melt pool shapes. Future bulk microstructure simulations should prioritize simulating as thick a deposit as possible, with large enough non-build dimensions for "steady state" behavior in the non-build directions.

Additionally, the assumption that grains that have better aligned [001] poles with the build direction will outcompete other grain orientations artificially forces a weak {001} texture. While this appears to work well with the standard single pass and lower energy density remelt strategies, i.e. 01, 02, 03, 04, 05, 07, 09, 11, it does not capture the shift to {011} textures for higher energy density remelt strategies, i.e. 06, 08, 12. The formation of {011} textures is dependent on accurate melt pool shapes and overlap/remelting patterns. Ongoing work with collaborators at CMU has demonstrated this capability with the current modeling approach. However, further optimization of the simulated melt pool shapes and orientation-dependent solidification model used in this work are necessary.

5. SUMMARY AND FUTURE OUTLOOK

This work successfully demonstrated the advantage of remelting to achieve higher density and target microstructures by expanding the narrow process window associated with LB-PBF. This approach can be highly valuable for austenitic stainless steels, which are not considered to be heat treatable, to tailor strength during fabrication. Remelt strategies targeting high density and fine grain sizes were promising suggesting further tunability may be possible. Remelting strategies targeting larger grain sizes, while successful must be balanced with the observed tendency towards stronger textures. The ability to simulate these processes would further enable optimization and the ability to downselect fewer scan strategies to experimentally investigate. The current computation model demonstrated some success in this area, but additional areas of improvement were identified in this work and are currently being addressed with collaborators from Carnegie Mellon University.

A logical path forward for this work is to leverage the remelt strategies to provide spatially gradient microstructures for stainless steel and other high impact AM materials. A spatially gradient approach can overcome one the biggest challenges associated with remelt strategies, the increased burden on process time. LB-PBF is an inherently slow manufacturing technique, compared to conventional manufacturing approaches, so additional increases to build time is not an ideal process. Utilizing a spatially gradient approach, however, can enable design engineers to select location dependent performance based on the service loading conditions Structural components are typically complex enough that geometrical features such as abrupt corners or through holes increase stress in local regions and are responsible for component failure in most instances. In these critical locations a remelt strategy can be utilized to provide improved strength and fatigue resistance while lower stress regions can utilize single pass scan strategies optimized to build rates rather than performance.

A key demonstrator of a spatially gradient approach would be design of a notched fatigue specimen utilizing remelt scan strategies to minimize porosity and reduce grain size ahead of the notch root to delay crack initiation. Beyond the high stress field of the notch root region, the remelt strategy could be adjusted to provide larger gain sizes capable of deflecting a propagating crack and further extending the life to failure. Furthermore, away from these regions influenced by the stress concentration or propagating crack scan strategies can be optimized for speed to improve the overall production time. Harmonizing the manufacturing of the material with design of component enables a level of design control not before realized and potentially provides improvements in mechanical performance beyond what is capable of conventional manufacturing.

REFERENCES

[1] A.B. Spierings, T.L. Starr, K. Wegener, Fatigue performance of additive manufactured metallic parts, Rapid prototyping journal (2013).
[2] A. Yadollahi, N. Shamsaei, Additive manufacturing of fatigue resistant materials: Challenges and opportunities, International Journal of Fatigue 98 (2017) 14-31.
[3] S. Romano, A. Brückner-Foit, A. Brandão, J. Gumpinger, T. Ghidini, S. Beretta, Fatigue properties of AlSi10Mg obtained by additive manufacturing: Defect-based modelling and prediction of fatigue strength, Engineering Fracture Mechanics 187 (2018) 165-189.
[4] E. Wycisk, A. Solbach, S. Siddique, D. Herzog, F. Walther, C. Emmelmann, Effects of defects in laser additive manufactured Ti-6Al-4V on fatigue properties, Physics Procedia 56 (2014) 371-378.
[5] B.C. Salzbrenner, J.M. Rodelas, J.D. Madison, B.H. Jared, L.P. Swiler, Y.-L. Shen, B.L. Boyce, High-throughput stochastic tensile performance of additively manufactured stainless steel, Journal of Materials Processing Technology 241 (2017) 1-12.
[6] R.R. Dehoff, M. Kirka, W. Sames, H. Bilheux, A. Tremsin, L. Lowe, S. Babu, Site specific control of crystallographic grain orientation through electron beam additive manufacturing, Materials Science and Technology 31(8) (2015) 931-938.
[7] J.W. Pegues, M.D. Roach, N. Shamsaei, Additive manufacturing of fatigue resistant austenitic stainless steels by understanding process-structure–property relationships, Materials Research Letters 8(1) (2020) 8-15.
[8] J.W. Pegues, M.D. Roach, N. Shamsaei, Effects of Postprocess Thermal Treatments on Static and Cyclic Deformation Behavior of Additively Manufactured Austenitic Stainless Steel, JOM 72(3) (2020) 1355-1365.
[9] J. Pegues, S. Shao, N. Shamsaei, N. Sanaei, A. Fatemi, D. Warner, P. Li, N. Phan, Fatigue of additive manufactured Ti-6Al-4V, Part I: The effects of powder feedstock, manufacturing, and post-process conditions on the resulting microstructure and defects, International Journal of Fatigue 132 (2020) 105358.
[10] J.C. Fox, S.P. Moylan, B.M. Lane, Effect of process parameters on the surface roughness of overhanging structures in laser powder bed fusion additive manufacturing, Procedia Cirp 45 (2016) 131-134.
[11] K.L. Johnson, T.M. Rodgers, O.D. Underwood, J.D. Madison, K.R. Ford, S.R. Whetten, D.J. Dagel, J.E. Bishop, Simulation and experimental comparison of the thermo-mechanical history and 3D microstructure evolution of 304L stainless steel tubes manufactured using LENS, Computational Mechanics 61(5) (2018) 559-574.
[12] J.W. Pegues, N. Shamsaei, M.D. Roach, R.S. Williamson, Fatigue life estimation of additive manufactured parts in the as-built surface condition, Material Design & Processing Communications 1(3) (2019) e36.
[13] B. Whip, L. Sheridan, J. Gockel, The effect of primary processing parameters on surface roughness in laser powder bed additive manufacturing, The International Journal of Advanced Manufacturing Technology 103(9-12) (2019) 4411-4422.
[14] J. Gockel, L. Sheridan, B. Koerper, B. Whip, The influence of additive manufacturing processing parameters on surface roughness and fatigue life, International Journal of Fatigue 124 (2019) 380-388.

[15] S. Lee, J.W. Pegues, N. Shamsaei, Fatigue behavior and modeling for additive manufactured 304L stainless steel: The effect of surface roughness, International Journal of Fatigue 141 (2020) 105856.
[16] A.M. Roach, B.C. White, A. Garland, B.H. Jared, J.D. Carroll, B.L. Boyce, Size-dependent stochastic tensile properties in additively manufactured 316L stainless steel, Additive Manufacturing 32 (2020) 101090.
[17] J. Beuth, J. Fox, J. Gockel, C. Montgomery, R. Yang, H. Qiao, E. Soylemez, P. Reeseewatt, A. Anvari, S. Narra, Process mapping for qualification across multiple direct metal additive manufacturing processes, Solid freeform fabrication proceedings, Univ. Tex. Austin, 2013, pp. 655-665.
[18] J. Gockel, J. Beuth, Understanding Ti-6Al-4V microstructure control in additive manufacturing via process maps, Solid freeform fabrication proceedings, Univ. Tex. Austin, 2013, pp. 666-674.
[19] S.C. Jensen, B.C. White, A. Garland, M. Heiden, D.J. Saiz, B. Boyce, B.H. Jared, MetalAdditiveManufacturing of Lattice Structures: A Study of ProcessParametersand MechanicalPerformance, Sandia National Lab.(SNL-NM), Albuquerque, NM (United States), 2019.
[20] A.G. Demir, B. Previtali, Investigation of remelting and preheating in SLM of 18Ni300 maraging steel as corrective and preventive measures for porosity reduction, The International Journal of Advanced Manufacturing Technology 93(5-8) (2017) 2697-2709.
[21] B. Liu, B.-Q. Li, Z. Li, Selective laser remelting of an additive layer manufacturing process on AlSi10Mg, Results in Physics 12 (2019) 982-988.
[22] R. Shrestha, N. Shamsaei, M. Seifi, N. Phan, An investigation into specimen property to part performance relationships for laser beam powder bed fusion additive manufacturing, Additive Manufacturing 29 (2019) 100807.
[23] Specification for Control and Qualification of Laser Powder Bed Fusion Metallurgical Processes, MSFC-SPEC-3717 EM 20 MSFC Technical Standard, National Aeronautics and Space Administration, 2017.
[24] S. Plimpton, C. Battaile, M. Chandross, L. Holm, A. Thompson, V. Tikare, G. Wagner, E. Webb, X. Zhou, C.G. Cardona, Crossing the mesoscale no-man's land via parallel kinetic Monte Carlo, Sandia Report SAND2009-6226 1 (2009).
[25] T.M. Rodgers, J.D. Madison, V. Tikare, Simulation of metal additive manufacturing microstructures using kinetic Monte Carlo, Computational Materials Science 135 (2017) 78-89.
[26] Z. Sun, X. Tan, S.B. Tor, C.K. Chua, Simultaneously enhanced strength and ductility for 3D-printed stainless steel 316L by selective laser melting, NPG Asia Materials 10(4) (2018) 127-136.
[27] D.M. T. M. Rodgers, F. Abdeljawad, O. D. Underwood, J. D. Carroll, B. H. Jared, D. S. Bolintineanu, J. A. Mitchell and J. D. Madison, Simulation of Powder Bed Metal Additive Manufacturing Microstructures with Coupled Finite Difference-Monte Carlo Method, Additive Manufacturing (Submitted 2020).
[28] J.T. Pauza, WA; Rollett, AD, Computer Simulation of Microstructure Development in Powder-Bed Additive Manufacturing with Crystallographic Texture, Acta Materialia (Submitted 2020).

This page left blank

DISTRIBUTION

Email—Internal

Name	Org.	Sandia Email Address
Kevin Dowding	01544	kjdowdi@sandia.gov
Kyle Johnson	01558	kyljohn@sandia.gov
Deidre Hirschfeld	01832	dhirsch@sandia.gov
Todd Kustra	02170	twkustr@sandia.gov
John Moser	02170	jcmoser@sandia.gov
Derek Wartman	02347	dswart@sanida.gov
Nick Leathe	02441	nleathe@sandia.gov
Seethambal Mani	02492	ssmani@sandia.gov
Justin Serrano	02492	jserra@sandia.gov
Technical Library	01977	sanddocs@sandia.gov

This page left blank

This page left blank

Sandia National Laboratories